The Influence of Crack Length and Delamination Width on the Mode-III Energy Release Rate of Laminated Composites

András Szekrényes

Journal of Composite Materials 2011 45: 279
DOI: 10.1177/0021998310376097

The Influence of Crack Length and Delamination Width on the Mode-III Energy Release Rate of Laminated Composites

ANDRÁS SZEKRÉNYES*
Department of Applied Mechanics, Budapest University of Technology and Economics, Muegyetem rkp. 5, Building MM, H-1111 Budapest, Hungary

ABSTRACT: In this article, the modified split-cantilever beam (MSCB) is applied to investigate the dependence of the mode-III energy release rate (at crack initiation) on the crack length and the specimen width. The main goal of this study is to apply the same specimen geometry to both double-cantilever beam and end-notched flexure systems. The energy release rate of the specimen was calculated by an improved beam theory scheme, which was used to reduce the experimental data. The obtained results are comparable to those obtained by mode-I and mode-II tests, and they indicate the important role of the MSCB specimen. The results show that the energy release rate decreases significantly with the initial crack length and there is no crack length where the energy release rate becomes independent of it.

KEY WORDS: delamination, fracture, modified split-cantilever beam, mode-III crack.

INTRODUCTION

IN THE PAST YEARS, more research was performed for the investigation of the mode-III toughness of laminated composite materials. The available specimen types for the mode-III measurements have already been discussed in other papers [1,2]. We refer only to some of the relevant configurations.

One of the earliest mode-III test developments is the split-cantilever beam (SCB) [3–5] which incorporates the loading parallel to the delamination plane. In the SCB specimen the presence of the mode-II component is significant: it is more than 40% of the total energy release rate (ERR) [3]. In order to eliminate the significant mode-II component, the specimen was loaded by using very stiff blocks; see for example the work by Hwang

*E-mail: szeki@mm.bme.hu
Figure 5 appears in color online: http://jcm.sagepub.com

0021-9983/11/03 0279–16 $10.00/0 DOI: 10.1177/0021998310376097

and Hu [4]. Robinson and Song [6] proposed the loading scheme necessary to reduce the mode-II component. While implementing their idea, Sharif et al. [1] and Trakas and Kortschot [7] constructed a special rig (modified split-cantilever beam – MSCB) realizing a mode-III dominant fracture. The method was applied recently by Rizov et al. [8] for the testing of glass fiber-reinforced woven laminates including finite element analysis and experiments. A recent study about the MSCB rig was published by the author of this article [2] introducing the advantages and drawbacks of the test.

The anti-clastic plate bending (ACPB) has also been applied to the determination of the mode-III fracture toughness [9]. The method applies a rectangular plate with side grooves at the middle line of the plate and so the ACPB produces a pure in-plane shear field. In the work of Podczek [10], it has been shown that the critical stress intensity factor (of a pharmaceutical powder compact material) decreases significantly with the notch depth of the ACPB specimen.

The edge-crack torsion (ECT) specimen was developed by Lee [11]. It is considered to be a very important contribution to the mode-III fracture developments [12–16]. An important feature of the ECT specimen is that the compliance calibration (CC) method can be applied [2,9]. Although the effect of friction in the ECT test was proven to be insignificant [17], in a recent study Ratcliffe [18] showed some drawbacks: dependence of the critical ERR (CERR) on the crack length, deviation of the load–displacement curves from linearity, and damage of the specimen before delamination failure. Among others, the ECT test was applied by Pennas et al. [19], who showed (corresponding with the results by Ratcliffe [18]) that the mode-III CERR increases with the crack length. Recently, de Moura et al. [20] elaborated that the increase of the toughness with the crack length is due to the fact that the crack does not propagate uniformly between the loading pins and the damaged area at peak load increases with the initial crack length.

More recently, de Morais and Pereira [21] published the four-point bending plate (4PBP) system for mode-III fracture characterization of composites. This test setup is simpler than that of the ECT; however the ERR can be obtained only by a finite element model.

Although at this stage the ECT specimen is believed to be the most promising candidate for mode-III toughness testing, in this study the MSCB specimen is employed for the determination of the dependence of the mode-III ERR at crack initiation on the initial crack length and specimen width. Based on the experimental data available in the literature, it seems that the toughness depends on the system applied. It is important to note that the MSCB specimen is the only configuration which makes it possible to investigate the mode-III initiation toughness in a quite extended crack length range, like the standard mode-I and mode-II tests involved. While the common crack length ranges in the ECT and ACPB specimens are within 10–30 mm, in the MSCB rig it is possible to use a specimen with initial crack length between 40 and 160 mm. Finally, the MSCB specimen maintains the traditional beam-like geometry; so it is also convenient, for comparison purposes, to mode-I and mode-II test results.

MODIFICATION OF THE ORIGINAL MSCB CONFIGURATION

The MSCB specimen applies a special rig, which transfers the scissor load to each specimen arm through two points [1,2]. The load transfer of the MSCB specimen is demonstrated in Figure 1. The two rigs transfer a scissoring load to the specimen. Compared to the rig used in [1,7], substantial modifications were made. At the position of the specimen

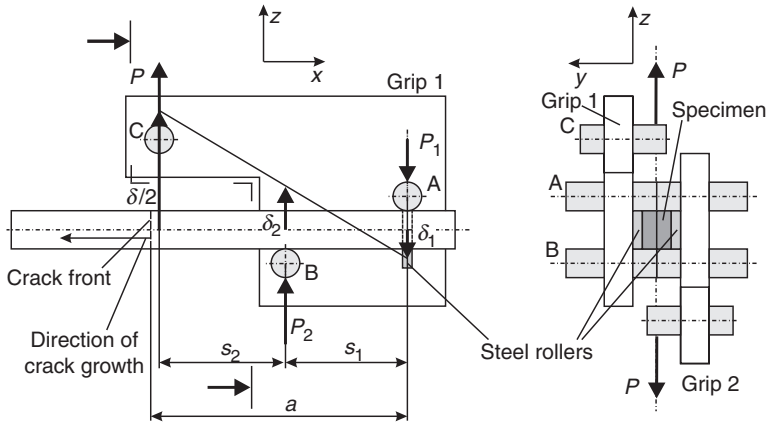

Figure 1. *Schematic illustration of the MSCB specimen.*

end (at roller A), the surface of the grip was grooved and a steel roller was inserted and glued to the surface of the grip (right side of Figure 1). The same modification was made for the other grip. The role of the steel rollers was to ensure that the cross-sections of the specimen arms at roller A do not rotate about x-axis, and to eliminate entirely the crack opening, which would induce a substantial increase in the mode-I ERR component. During testing, the specimen end was blocked by the two rollers and the loading grips were held in a given sideways (y) position. Furthermore, the loading rollers applied by Sharif et al. [1] were substituted with grub screws, which made it very easy to control and hold the loads in the right position by using a screwdriver. Finally, the torsional deformation of the specimen is not prevented in the modified rig shown in Figure 1 (in contrast with the original rig [1,7]), which involves the consideration of the free torsion effect in the specimen. Figure 2(a) shows the applied boundary conditions and loads, while Figure 2(b) shows the deformation of the specimen. Twisting is caused by the torque of the forces P_1 and P_2 with respect to the origin of the x–y–z coordinate system (Figure 2(b)). In the original configuration [1] the moment around x-axis was partly eliminated by the appropriate placement of roller B (shifting of roller B along y-axis); however this requires some care since due to the relatively small thickness ($h = 3.1$ mm) of the specimen it can lead to the crush of the arms under the loading noses. On the other hand, to prevent entirely the specimen twisting in the original rig, the specimen was constrained between the side plates; however this can lead to undesired frictional effects. In the modified rig, the steel rollers ensure that there is no contact (and no friction) between the specimen and the loading grips during the torsional deformation shown in Figure 2(b). By varying the diameter of the steel rollers, it is possible to test specimens with relatively high angle of twists.

The 3D view of the applied equipment and the most important details are given in Figure 3 developed in SOLIDWORKS. The load was transferred by the load transferring plates (3), which were held in a given sideways position by using the wedge grips (4) of the testing machine. The blocks were inserted to the loading plates preventing the rotation around x-axis and even the displacement in the y-direction of the loading plates during testing. The loading grips (2) were free to rotate around the y-axis, which was made by using the shafts (5) shown in Figure 3(b). Since the plates transfer two loads of which influence lines do not coincide, the distance between them produces a moment about

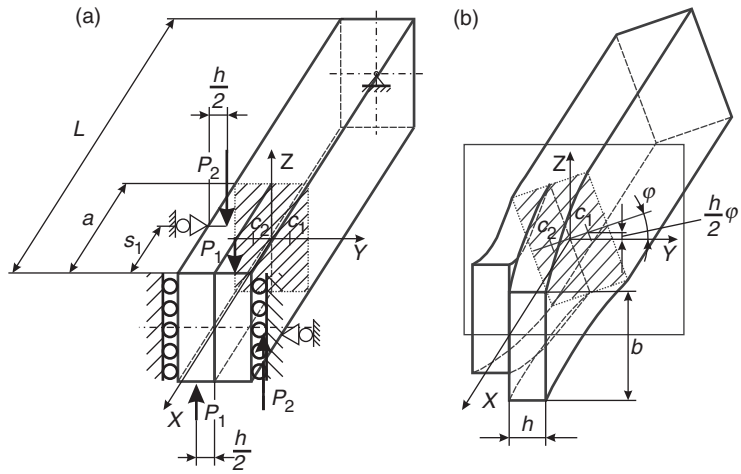

Figure 2. *(a) The boundary conditions and loads, (b) deformation of the MSCB specimen.*

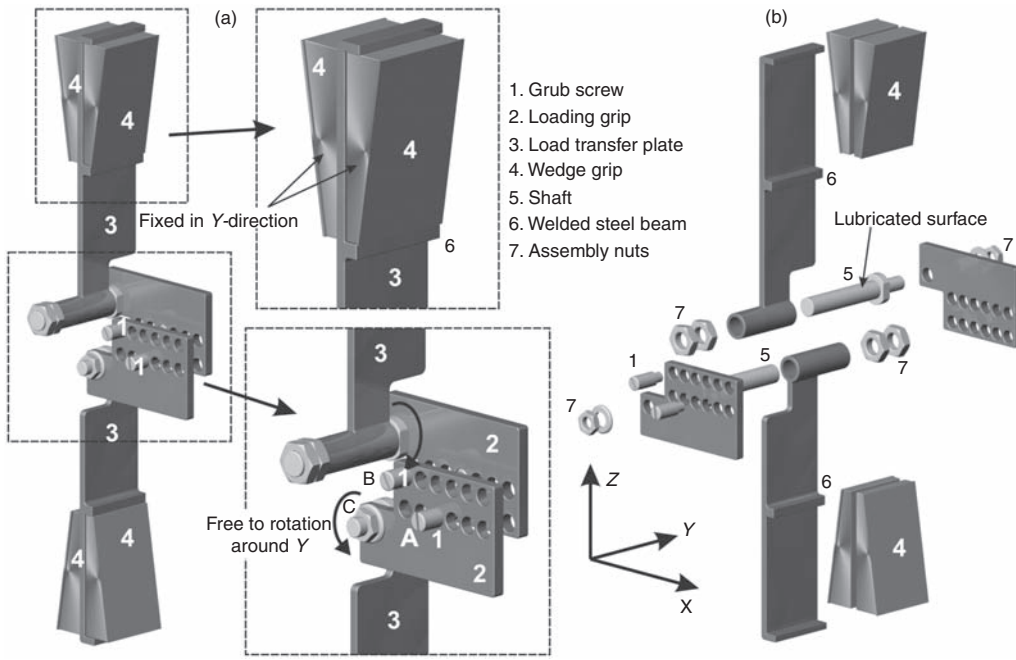

Figure 3. *The 3D view of the experimental equipment: (a) assembled state and (b) exploded view.*

x-axis. This moment is completely transferred to the shafts and so, theoretically the specimen was loaded only by forces (P_1 and P_2 in Figure 1) through the four grub screws. Using this equipment, it is possible to reduce the load of the specimen to a beam problem subjected to the basic types of load [2]. In the following sections, we present the details and the results of the experiments performed by using the rig in Figure 3.

EXPERIMENTS

The constituent materials of the E-glass/polyester composite were procured from Novia Ltd. The properties of the E-glass fiber are $E = 70$ GPa and $\nu = 0.27$, and the properties of the unsaturated polyester resin we applied are: $E = 3.5$ GPa and $\nu = 0.35$. Both were considered to be isotropic. The unidirectional ($[0^\circ]_{14}$) E-glass/polyester specimens with thickness of $2h = 6.2$ mm, width of $b = 9$, 12.5, 14.5, and 20 mm, and fiber-volume fraction of $V_f = 43\%$ were manufactured in a special pressure tool. A polyamide (PA) insert with thickness of 0.03 mm was placed at the midplane of the specimens to make an artificial starting defect. A great advantage of the present E-glass/polyester material is transparency, which makes it possible to observe the crack initiation visually. The tool was left at room temperature until the specimens became dry. Then the specimens were removed from the tool and were further left at room temperature for 4–6 h. The specimens were cut to the desired length and were precracked in an opening mode of 4–5 mm by using a sharp blade. The MSCB specimen is suitable only for the crack initiation measurement, because the mode ratio changes with the crack length [2].

Material Properties and Geometrical Parameters

The flexural modulus of the material was determined from a three-point bending test with span length of $2L = 150$ mm using six uncracked specimens with $2h = 6.2$ mm and $b = 20$ mm. The flexural modulus was calculated based on the slope of the measured load–displacement curves using a simple beam theory expression. Then the specimens were cut along the longitudinal direction in order to obtain very narrow specimens. The narrow specimens were rotated by 90° about the longitudinal axis compared to the original measurements and the slope of the load–displacement curve was calculated; the modulus of the specimens was determined from a simple beam theory expression again. Both experiments resulted in $E_{11} = 33$ GPa, that is, the material was found to be transversely isotropic. The additional properties were predicted by using simple rule of mixture; in this way, $E_{22} = E_{33} = 7.2$ GPa, $G_{12} = G_{13} = 3$ GPa, and $\nu_{12} = \nu_{13} = 0.27$ were obtained. The material properties were used only in the data reduction process.

To investigate the influence of the initial crack length and the specimen width on the mode-III ERR at crack initiation, a large number of experiments was performed. When the crack front coincides with the axis of external loading, there is no bending moment on the specimen arms, and this reduces the mode-II component of the ERR at the upper and lower surfaces. As the crack grows away from the loading axis, the mode-II component builds up, so that the mode of crack growth is no longer pure mode-III. The condition of at least a 96% mode-III dominant test is [2]:

$$1.02 \leq \frac{a}{s_1 + s_2} \leq 1.09. \tag{1}$$

Finite element calculations show that the mode-III dominance holds if Equation (1) is satisfied [2]. Table 1 shows the geometrical parameters of the specimens tested. At each crack length four measurements were performed, which means – based on Table 1 – a total of $24 \times 4 = 96$ measurements. Table 1 also shows the values of s_1 and s_2 and the ratio given by Equation (1), and as it is shown in two cases, Equation (1) was violated (if $b = 9$ mm and $a = 42$ and 70 mm). Actually, that means a 94% mode-III condition instead of 96%.

Table 1. The geometrical parameters of the MSCB test and the results of the DBT scheme.

$b = 9$ mm	a (mm)	42	55	70	80	95	100	105	120	130	130	148
	s_1 (mm)	13.0	26.0	38.0	41.4	42.1	51.8	65.2	65.5	65.7	79.9	80.0
	s_2 (mm)	25.0	25.0	25.0	37.0	48.4	42.8	32.6	46.2	59.7	47.1	63.0
	$s_1 + s_2$	38.0	51.0	63.0	78.4	90.5	94.6	97.8	111.7	125.4	127.0	143.0
	$a/(s_1 + s_2)$	1.11	1.08	1.11	1.02	1.05	1.06	1.02	1.07	1.04	1.02	1.03
	DBT G_{IIIQ} ($\mathrm{J/m^2}$)	375.1	267.3	251.6	163.2	124.2	153.2	133.4	132.3	88.4	97.1	63.4
	Scatter	±72.8	±22.7	±29.6	±35.8	±11.2	±20.5	±6.6	±11.8	±9.1	±17.1	±3.6
$b = 12.5$ mm	a (mm)	90	95	105	120	135	150					
	s_1 (mm)	49.8	40.1	49.3	64.1	78.6	78.7					
	s_2 (mm)	35.1	52.9	51.2	51.0	52.1	66.5					
	$s_1 + s_2$	84.9	93.0	99.1	115.1	130.7	145.2					
	$a/(s_1 + s_2)$	1.06	1.02	1.06	1.04	1.03	1.03					
	DBT G_{IIIQ} ($\mathrm{J/m^2}$)	152.0	115.2	100.5	112.4	92.1	68.7					
	Scatter	±17.6	±11.4	±16.3	±5.1	±7.5	±7.8					
$b = 14.5$ mm	a (mm)	90	95	105	120	135	150					
	s_1 (mm)	48.6	52.3	48.3	63.3	77.6	77.9					
	s_2 (mm)	38.0	41.2	53.6	53.3	54.7	68.9					
	$s_1 + s_2$	86.6	93.5	101.1	116.6	132.3	146.8					
	$a/(s_1 + s_2)$	1.04	1.02	1.04	1.03	1.02	1.02					
	DBT G_{IIIQ} ($\mathrm{J/m^2}$)	131.3	129.3	103.2	93.5	67.6	56.1					
	Scatter	±9.0	±2.2	±6.2	±3.9	±5.1	±3.9					
$b = 20.0$ mm	a (mm)	155										
	s_1 (mm)	75.0										
	s_2 (mm)	75.0										
	$s_1 + s_2$	150.0										
	$a/(s_1 + s_2)$	1.03										

For the measurements, two different grips were used: a small one where the distance between the axis of the grub screws was 19 mm and a large one, where the axis of the grub screws was located to a distance of 30 mm from each other. The thread was turned to a diameter of 10 mm at the end of the grub screws. That means actually that the contact distance between the rollers is 9 mm in the small grip and it is 20 mm in the large grip if the grips are located in a position given by Figure 1.

The small grip was used to perform tests on 9, 12.5, and 14.5 mm wide specimens in the $a = 42, \ldots, 90$ mm crack length range, while the large grip was suitable to test 9, 12.5, 14.5, and 20 mm wide specimens in the crack length range of $a = 95, \ldots, 155$ mm. If the width of the specimen and the distance between the grub screws' contact points were different, then the arising gap between the grub screws and the specimen sides was eliminated by rotating the grips about point C and moving the grips in vertical direction until the gap was closed. This process involves the alteration of the distances s_1 and s_2, which is demonstrated in Figure 4, where it is shown that s_1 and s_2 should be corrected in accordance with the specimen width. The initial values s_{10} and s_{20} are known, as well as the vertical distances z_{A0} and z_{B0} for both grips, respectively. The details of the geometrical correction are given in Appendix. Table 1 contains the corrected s_1 and s_2 lengths.

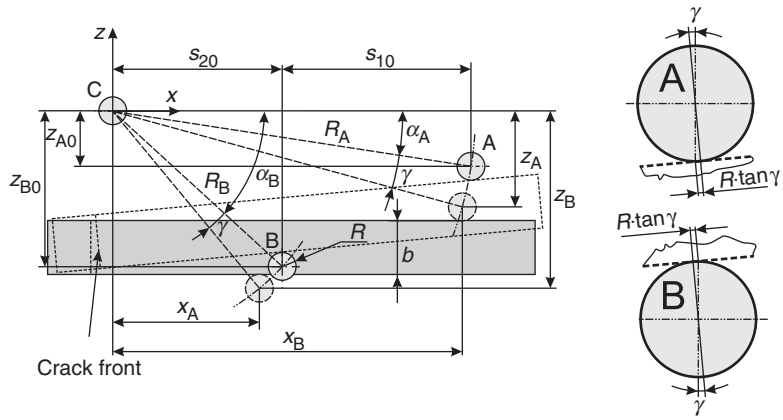

Figure 4. *Correction scheme for the MSCB specimen.*

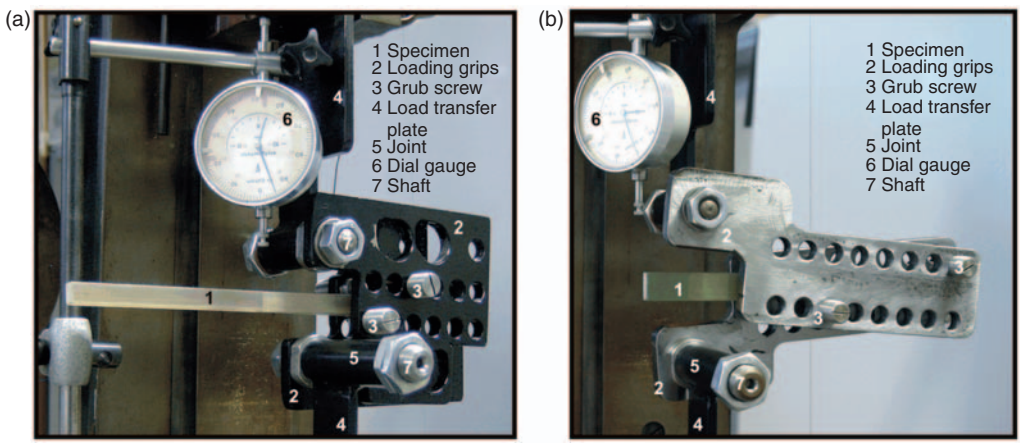

Figure 5. *The experimental equipment for the mode-III MSCB specimen: (a) small rig and (b) large rig.*

Data Recording and Reduction

During the tests, the specimens were put into the loading grips shown in Figure 5. Then the specimens were loaded subsequently, and the load and displacement values were read from the scale of the testing machine and using the mechanical dial gauge shown in Figure 5(a) and (b) (number 6). The crack initiation was identified visually (the specimens were transparent). The measured data were evaluated by a validated improved beam theory (IBT) scheme [2]. Based on the analysis, the compliance of the MSCB specimen at roller C is [2]:

$$C = \frac{8a^3}{b^3 h E_{11}} [f_{\mathrm{EB1}} + f_{\mathrm{TIM1}} + f_{\mathrm{FT1}} + f_{\mathrm{S-V1}}], \tag{2}$$

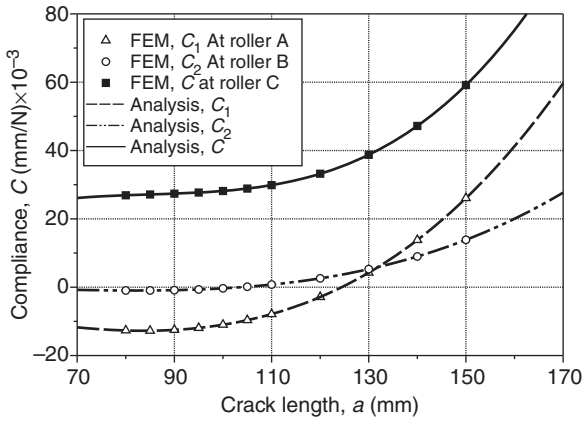

Figure 6. *Comparison of the compliances by finite element method and beam theory.*

where:

$$f_{\mathrm{EB1}} = 1 - 3\left(\frac{s_1 + s_2}{a}\right) + 3\left(\frac{s_1 + s_2}{a}\right)^2 - \frac{s_1(s_1 + s_2)(s_1 + 2s_2)}{a^3}, \tag{3}$$

$$f_{\mathrm{TIM1}} = 0.3\left(1 - \frac{s_2^2 - s_1^2}{as_1}\right)\left(\frac{b}{a}\right)^2\left(\frac{E_{11}}{G_{13}}\right), \tag{4}$$

$$f_{\mathrm{FT1}} = 0.19\frac{1}{\varsigma}\left(1 - \frac{s_1}{a}\right)\left(\frac{b}{a}\right)^2\left(\frac{E_{11}}{G_{12}}\right), \tag{5}$$

$$f_{\mathrm{S-V1}} = 0.48\left(\frac{a - (s_1 + s_2)}{a}\right)^2\left(\frac{b}{a}\right)\left(\frac{E_{11}}{G_{13}}\right)^{\frac{1}{2}}, \tag{6}$$

where a is the crack length, b the specimen width, h the half of the specimen thickness, E_{11} the flexural modulus, G_{12} and G_{13} the shear moduli in the x–y and x–z plane, and s_1 and s_2 are the distances between the loading rollers A, B, and C, respectively (Figure 1). The factors consider the following deformations: f_{EB1} – bending, f_{TIM1} – shear, f_{FT1} – free torsion, and $f_{\mathrm{S-V1}}$ – Saint-Venant effect. The analytical solution was compared to finite element calculations and a very good agreement was found. Figure 6 shows the analytical and numerical compliances if the geometrical properties are: $b = 9$ mm, $2h = 6.2$ mm, $s_1 = 41$ mm, and $s_2 = 49$ mm in the crack length range of $a = 70$–150 mm. C is the compliance at roller C, C_1 the compliance at roller A, and C_2 is the compliance at roller B. The total compliance, C is based on the linear interpolation (Figure 1) of C_1 and C_2. As it is shown, the agreement is quite good, which shows the accuracy of the analytical model. The ERR of the MSCB specimen is given by [12]:

$$G_{\mathrm{MSCB}} = \frac{P^2}{2b}\frac{\mathrm{d}C}{\mathrm{d}a}, \tag{7}$$

which results in:

$$G_{\mathrm{MSCB}} = \frac{12P^2a^2}{b^4hE_{11}}[f_{\mathrm{EB2}} + f_{\mathrm{TIM2}} + f_{\mathrm{FT2}} + f_{\mathrm{S-V2}}], \tag{8}$$

where P is the applied load. Furthermore:

$$f_{\mathrm{EB2}} = 1 - 2\left(\frac{s_1 + s_2}{a}\right) + \left(\frac{s_1 + s_2}{a}\right)^2, \tag{9}$$

$$f_{\mathrm{TIM2}} = 0.1\left(\frac{b}{a}\right)^2\left(\frac{E_{11}}{G_{13}}\right), \tag{10}$$

$$f_{\mathrm{FT2}} = 0.06\frac{1}{\varsigma}\left(\frac{b}{a}\right)^2\left(\frac{E_{11}}{G_{12}}\right), \tag{11}$$

$$f_{\mathrm{S-V2}} = 0.32\left(1 - \frac{s_1 + s_2}{a}\right)\left(\frac{b}{a}\right)\left(\frac{E_{11}}{G_{13}}\right)^{1/2}, \tag{12}$$

$$\varsigma = 1 - 0.63\mu\frac{h}{b}, \mu = \left(\frac{G_{13}}{G_{12}}\right)^{1/2}. \tag{13}$$

In accordance with direct beam theory (DBT) it is possible to obtain the following scheme for the MSCB specimen [2]:

$$G_{\mathrm{DBT}} = \frac{3P\delta}{2ba}\left(\frac{f_{\mathrm{EB2}} + f_{\mathrm{TIM2}} + f_{\mathrm{FT2}} + f_{\mathrm{S-V2}}}{f_{\mathrm{EB1}} + f_{\mathrm{TIM1}} + f_{\mathrm{FT1}} + f_{\mathrm{S-V1}}}\right), \tag{14}$$

where the coefficients in the parentheses are given by Equations (3)–(6) and Equations (9)–(12). In Equation (14), P and δ are the experimentally measured load and displacement values at roller C at the point of crack initiation.

The material used in this study was transparent and it was very easy to identify the crack initiation at any crack length. The crack initiation was identified with an accuracy of 0.5 mm, and although the mode ratio changes as the crack grows, a small increment like this does not cause significant changes and so it was neglected. For example, if the crack lengths are $a = 55$ mm and $s_1 = 26$ mm, $s_2 = 25$ mm and we assume a 1 mm crack increment at initiation, then $a/(s_1 + s_2) = 56/51 = 1.098$, which in fact violates Equation (1) but it is still a 94–95% mode-III test [2].

The distribution of the ERR along the crack front was investigated in [2], and it was shown that the mode-III ERR has a distribution similar to that of the DCB specimen, i.e., the ERR is the highest at the center of the specimen, and it is the smallest at the specimen sides. The mode-II component is zero at the center and it is highest (but relatively small) at the specimen sides and decays very fast to near zero. This means that the fracture mode near the center of the specimen is pure mode-III, and in each case presented in Table 1 the crack initiation occurred at the center of the crack front or in the small vicinity of the center point. This aspect is discussed in [2].

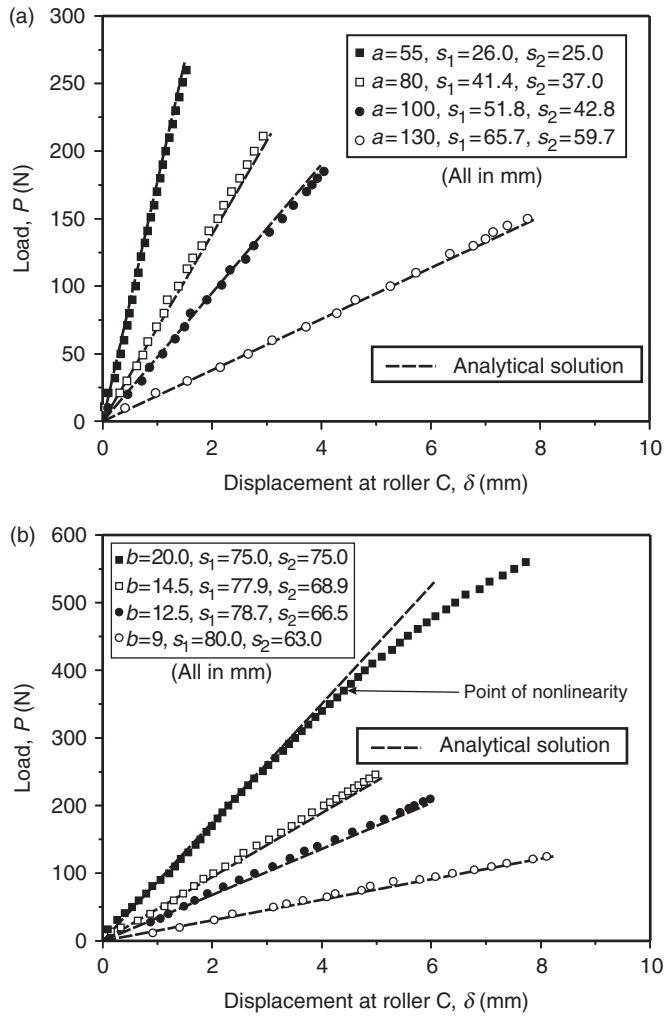

Figure 7. *Load–displacement curves up to fracture initiation: (a) for the* $b = 9$ *mm wide specimens and (b) for the specimens with the longest crack length.*

RESULTS AND DISCUSSION

Figure 7(a) demonstrates the measured load–displacement curves up to fracture initiation including several crack lengths if $b = 9$ mm. Crack initiation occurred at the end of the curves, and the initiation was identified visually in the transparent specimens. Figure 7(b) collects the load–displacement curves for the case of $b = 9$, 12.5, 14.5, and 20 mm and $a = 148$, 150, 150, and 155 mm. In each case, the dashed line shows the corresponding analytical solution, which was obtained by using the $P = \delta/C$ relationship based on Equation (2). The response was essentially linear elastic; the deviation from the analytical curves is absolutely negligible. The only exception is the case of the 20 mm wide specimen with $a = 155$ mm, where the response became nonlinear and no crack initiation was observed before the point of nonlinearity (shown in Figure 7(b)). After removing the

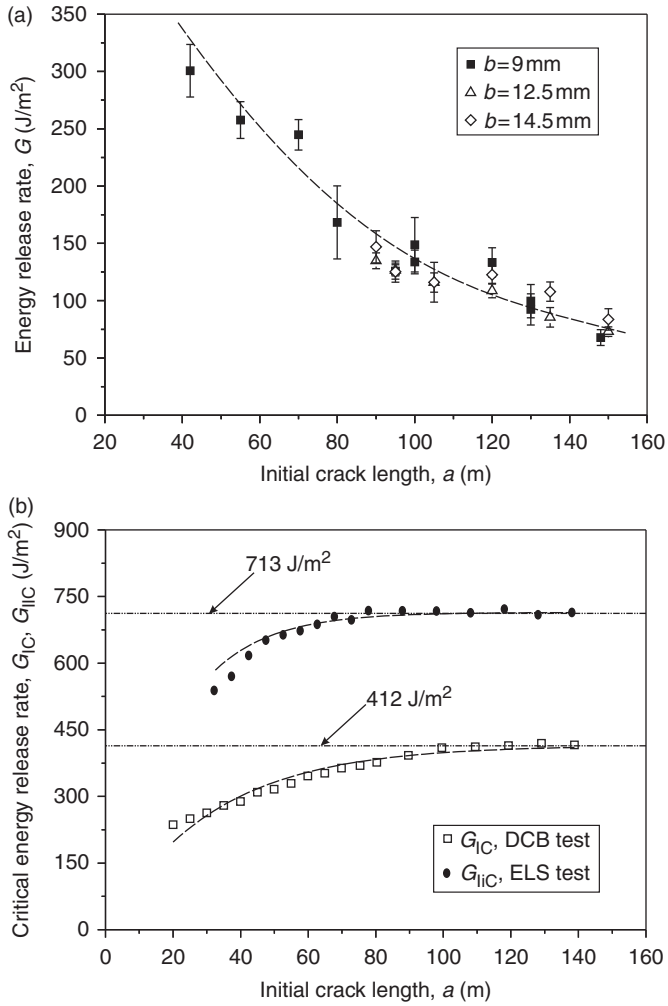

Figure 8. *The mode-III ERR at crack initiation (G_{IIIQ}) as the function of the initial crack length measured by the MSCB specimen (a) and the dependence of the mode-I and (b) mode-II CERRs at crack initiation on the initial crack length based on DCB [26] and ELS [27] measurements.*

20 mm wide specimens from the testing machine, it was observed that the specimen sides were crushed due to the contact deformation between the grub screws and the specimen sides. This is a certain limitation of the test. Furthermore, by increasing the specimen width, the stiffness of the specimen increases significantly and much higher force is needed to initiate the crack. Overall, Figure 7 shows the accuracy of the beam model.

The reduced experimental data are plotted in Figure 8(a). The ERR at crack initiation (denoted as G_{IIIQ}) decreases significantly with the initial crack length and it is approximately independent of the specimen width, since the data of the 12.5 and 14.5 mm wide specimens fall into the same range as those of the 9 mm wide ones. The latter was also observed by Robinson and Song [6]. The experimentally determined ERR (G_{IIIQ}) decreases from 300 to 70 J/m^2 (with a maximum deviation of 23 J/m^2) in the crack length range of

42–150 mm. In spite of that, it was not possible to identify an asymptotic value, where the ERR becomes independent of the crack length. Therefore, the energy release rate values in Figure 8(a) are marked as G_{IIIQ}, which are determined experimentally, although they do not represent the critical values (G_{IIIC}), because G_{IIIC} is a material property. It is possible that in the crack tip region there are micro-processes (e.g., plastic deformation), which are not captured by the IBT scheme. A possible solution could be the application of the cohesive zone models [22,23], which apply nonlinear springs in the crack tip region.

In Table 1, the results of the DBT scheme are collected in the last rows. It must be highlighted again, that the experimentally determined ERR is denoted by G_{IIIQ} due to the significant crack length dependence. The difference between IBT and DBT is notable only at $a = 42$ mm ($b = 9$ mm), which is probably due to the relatively high bending stiffness of the specimen. But as it can be seen that if $a = 55$ mm, then the stiffness is already appropriately low for the application of beam theory. In a previous work [24], the mode-III ERR at crack initiation was measured to be 445 J/m^2 at $a = 55$ mm and $b = 9$ mm using the MSCB system and the same material. In contrast, $G_{IIIQ} = 267.3$ J/m^2 was obtained with $b = 9$ mm and $a = 55$ mm (Table 1). This can be explained by the significant modifications of the test setup: the net moment around x-axis is transferred to the shafts and the loading plates, while the frictional effect is also eliminated/reduced by the lubrication of the shafts (number 5 in Figure 3).

The CERR-a data (at crack initiation) by mode-I double-cantilever beam (DCB) [25] and mode-II end-loaded split (ELS) [26] tests in Figure 8(b) for the same material indicate that the mode-III crack behaves completely in the opposite way as that of mode-I and mode-II cracks. Under mode-I and mode-II cases, a plateau value is reached and it could be assumed (based on Figure 8(b)) that the CERRs are independent on the initial crack length, i.e., they are material properties. A behavior of similar to that shown in Figure 8(b) was observed also by Hashemi et al. [25]. The obtained results involve the following conclusions:

1. G_{IIIC} is assumed to be a material property, and therefore it cannot be measured by this test or the data reduction method is not appropriate.
2. The determined mode-III ERR (G_{IIIQ}) is independent of the specimen width.
3. In specimens with longer cracks ($a > 60$ mm) the mode-III ERR measured by the MSCB test (G_{IIIQ}) is less than the mode-I and even the mode-II CERR, i.e., $G_{IIIQ} < G_{IC} < G_{IIC}$.
4. The mode-III ERR depends on the configuration applied for testing.

Table 2 presents a short overview of the mode-III experimental results performed by other researchers. In each case, the ERR at crack initiation is measured. Based on the available experimental data in the literature, the mode-III ERRs measured by the ECT test are much higher than the one for the material used in this study [16,18]. Although this can be attributed to the different material properties and the specimen lay-up, all the authors who applied the ECT test experienced an increasing ERR with the initial crack length. On the contrary using the ACPB test Podczek [10] (last two rows in Table 2) observed a behavior similar to the results of this study, although not in composite materials. But it can be assumed that a behavior similar to that is possible also in composites. It should be mentioned that Hwang and Hu [4] experienced also a behavior similar to that of the material used in this study; however the number of points measured by the SCB test was not enough to draw major conclusions. Overall, all these authors experienced the dependence of the mode-III ERR on the crack length.

Table 2. Experimental results of the mode-III fracture tests for laminated composite materials.

Conf.	Authors, Year	$L{\cdot}b$ [mm·mm]	a/b or a [mm]	Material type, Specimen lay-up	V_f [%]	Thickness t (mm)	Reduction method	Crossh. rate (mm/min)	G_{II} [J/m^2]	G_{IIIC} [J/m^2] K_{IIIC} [MNm$^{3/2}$]
ECT	Pennas et al., 2007	76·32	0.2…0.7	glass/polypropylene [90,0,+45,−45,−45,+45,0,90]	35	4.7	CC	2	1570	2800…4000 J/m^2
ECT	Pennas et al., 2007	76·32	0.2…0.7	woven glass/epoxy [90/0,(+45/−45)2/−45/+45)20/90]S	45	6.5			–	1600…3200 J/m^2
ECT	Ratcliffe, 2004	76·32	0.2…0.6	IM7/8552 carbon epoxy [90/0(+45/−45)2/(−45/+45)2/0/90]S	60	4.5	CC	1.3	1334	900…1300 J/m^2 (average: 1110 J/m^2)
ECT	Ratcliffe, 2004	76·32	0.2…0.6	S2/8552 glass epoxy [90/0(+45/−45)3/(−45/+45)3/0/90]S	60	7.5			1759	1000…2200 J/m^2 (average: 1416 J/m^2)
ECT	Liao and Sun, 1996	280·50	7.8…14.1	AS4 3501-6 graphite epoxy [0/90]10S	–	5.2	Analytical series solution	–	$\cong G_{III}$	772…850 J/m^2 (average: 846 ± 82 J/m^2)
ECT	Liao and Sun, 1996	280·50	9.1…14.3	AS4 3501-6 graphite epoxy [0/90]10S	–	5.6				737…945 J/m^2 (average: 800 ± 65 J/m^2)
ECT	Liao and Sun, 1996	280·50	3.3…4.3	AS4 3501-6 graphite epoxy [+−15]8S]	–	4.4				682…738 J/m^2 (average: 724 ± 32 J/m^2)
ECT	Liao and Sun, 1996	280·50	1.0…1.13	AS4 3501-6 graphite epoxy [+−15]10S]	–	5.4				600…742 J/m^2 (avergae: 665 ± 52 J/m^2)
ECT	Liao and Sun, 1996	280·50	9…11.6	AS4 3501-6 graphite epoxy [+−45]10S]	–	5.6				569…703 J/m^2 (average: 653 ± 51 J/m^2)
ECT	Li et al., 2004	83·38	0…22.9	glass epoxy [90/(+−45)4/(−+45)4/90]S	56	8.2	CC	1.27	–	500…2500 J/m^2 (average:1480 ± 180 J/m^2)
ECT	Li et al., 2004	83·38	0…22.9	glass epoxy [90/(+−45)5/(−+45)5/90]S	26	12	CC	1.27	–	3790 ± 790 J/m^2 1000…6500 J/m^2 (average: 4200 ± 560 J/m^2)
SSCB 80%	Hwang and Hu, 2001	280·25	40, 60, 80	24 ply carbon-epoxy, HTA 1200A/ACD8801 unidirectional	60	3	CC, FEM	0.5	–	1800, 1000, 1600 J/m^2
ACPB	Podczek, 2001	20·20	1…9	acetylsalicylic acid	–	5	Plate theory	1	–	390…5 MNm$^{3/2}$
ACPB	Podczek, 2001	20·20	1…9	lactose monohydrate	–				–	240…5 MNm$^{3/2}$

The ECT and MSCB specimens show a completely opposite ERR dependence on the initial crack length. In accordance with Pennas et al. [19], the mode-III ERR increases from 1600 to 3200 J/m^2 within the crack length range of $a = 6.4, \ldots, 22.4$ mm. That means a 100% increase within 16 mm. On the other hand, G_{IIIQ} decreases from 320 to 250 J/m^2 within $a = 40 \ldots 60$ mm in accordance with Figure 8(a), which is a 22% decrease. However, it is possible that there is a transition zone, and after an initial increase (in accordance with the ECT specimen) the ERR decreases with the crack length (according to the results of the MSCB tests). A significant difference between the ECT and MSCB specimens is that the ECT applies a relatively wide specimen with small crack lengths, while the MSCB is applicable only for relatively slender beams with long crack lengths. In many studies, the mode-III ERR obtained from the ECT test was compared to the mode-I and mode-II CERRs; however it has not been considered that the mode-III ERR depends on the crack length; so it is reasonable to evaluate the ERRs at the same crack length under different modes.

To clarify the above-mentioned contradictions and questions more number of experiments are necessary. First of all, a comparison between the results of the ECT and MSCB tests for the same material is essential. On the other hand, a new data reduction scheme should be developed, because although the IBT scheme excellently captures the deformation of the specimen, it seems to be inaccurate to calculate realistic ERRs in the MSCB specimen. Probably this will be discussed in a future paper.

CONCLUSIONS

In this article, the dependence of the mode-III ERR at crack initiation on the initial crack length and specimen width was investigated by using the MSCB specimen. A small grip and a large grip were applied for the experiments to determine the mode-III energy release rate in an extended crack length range ($a = 42, \ldots, 150$ mm). It was found that there are some limitations concerning the geometrical properties of the specimens, i.e., if the initial crack length is too short, or the stiffness of the specimen is too high, the crack cannot be initiated and a damaged (crushed) zone around the loaded boundaries can be expected due to the high contact pressure prior to crack onset. Apart from these limitations, it was elaborated that the mode-III ERR decreases significantly with the initial crack length and this is in a sharp contrast with those results which were obtained by using edge-cracked torsion tests, where a significant increase with the initial crack length was found. However, the major difference between the modified split-cantilever and edge-cracked torsion tests is the crack length range available for testing. Anyway, both tests show that the mode-III energy release rate at crack initiation depends on the geometry of the specimen and the configuration applied for testing. Consequently, the determined energy release rate at crack initiation is not the critical value, because that is independent on the specimen geometry; in other words G_{IIIC} is a material property. In this respect, the next step could be the conduction of edge-cracked torsion and MSCB tests for the same material.

APPENDIX

The radii R_{A} and R_{B} given in Figure 4 are:

$$R_{\mathrm{A}} = \sqrt{z_{\mathrm{A0}}^2 + (s_{10} + s_{20})^2}, \quad R_{\mathrm{B}} = \sqrt{z_{B0}^2 + s_{20}^2}, \tag{A.1}$$

where s_{10} and s_{20} are the initial locations of rollers A and B, $z_{A0} = 17$ mm, $z_{B0} = 36$ mm for the small grip and $z_{A0} = 15$ mm, $z_{B0} = 45$ mm for the large grip. The angles α_A and α_B based on Figure 4 are:

$$\alpha_A = \arctan\frac{z_{A0}}{s_{10} + s_{20}},\ \alpha_B = \arctan\frac{z_{B0}}{s_{20}}. \tag{A.2}$$

The distances x_A, z_A, x_B, and z_B are expressed as:

$$\begin{aligned} x_A &= R_A\cos(\alpha_A + \gamma),\ z_A = R_A\sin(\alpha_A + \gamma), \\ x_B &= R_B\cos(\alpha_B + \gamma),\ z_B = R_B\sin(\alpha_B + \gamma), \end{aligned} \tag{A.3}$$

where γ is the angle of rotation of the grips about roller C for a given specimen width, b in order to eliminate the gap among the grub screws and the specimen boundaries. To obtain γ a transcendent equation should be solved:

$$z_B - z_A = R_B\sin(\alpha_B + \gamma) - R_A\sin(\alpha_A + \gamma) = b + 2R. \tag{A.4}$$

In accordance with Figure 4 the distances s_1 and s_2 are:

$$s_1 = x_A - x_B + 2R\tan\gamma,\ s_2 = x_B - 2R\tan\gamma, \tag{A.5}$$

where the last terms are necessary due to the fact that the contact points of rollers A and B are shifted with a distance of $R{\cdot}\tan\gamma$ compared to the vertical axis, as it is shown in the right-hand side of Figure 4.

ACKNOWLEDGMENTS

This study was supported by the János Bolyai Research Scholarship of the Hungarian Academy of Sciences and the National Science and Research Fund (OTKA) under Grant No. T34040.

REFERENCES

1. Sharif, F., Kortschot, M.T. and Martin, R.H. (1995). Mode III Delamination Using a Split Cantilever Beam, In: Martin, R.H. (ed.), *Composite Materials: Fatigue and Fracture*, Vol. 5, pp. 85–99, ASTM STP 1230, ASTM, Philadelphia.
2. Szekrényes, A. (2009). Improved Analysis of the Modified Split-Cantilever Beam for Mode-III Fracture, *International Journal of Mechanical Sciences*, **51**: 682–693.
3. Donaldson, S.L. (1988). Mode III Interlaminar Fracture Characterization of Composite Materials, *Composites Science and Technology*, **32**: 225–249.
4. Hwang, S.-F. and Hu, C.-L. (2001). Tearing Mode Interlaminar Fracture Toughness of Composite Materials, *Polymer Composites*, **22**: 57–64.
5. Naik, N.K., Reddy, K.S., Meduri, S., Raju, N.B., Prasad, P.D., Azad, Sk.N.M., Ogde, P.A. and Reddy, B.C.K. (2002). Interlaminar Fracture Characterization for Plain Weave Fabric Composites, *Journal of Material Science*, **37**: 2983–2987.
6. Robinson, P. and Song, Q.D. (1994). The Development of an Improved Mode III Delamination Test for Composites, *Composite Science and Technology*, **52**: 217–233.
7. Trakas, K. and Kortschot, M.T. (1997). The Relationship Between Critical Strain Energy Release Rate and Fracture Mode in Multidirectional Carbon-Fiber/Epoxy Laminates, In: Armanios, E.A. (ed.), *Composite Materials: Fatigue and Fracture*, Vol. 6, pp. 283–304, ASTM STP 1285, ASTM, Philadelphia.

8. Rizov, V., Shindo, Y., Horiguchi, K. and Narita, F. (2006). Mode III Interlaminar Fracture Behaviour of Glass Fiber Reinforced Polymer Woven Laminates at 293 to 4 K, *Applied Composite Materials*, **13**: 287–304.
9. Farshad, M. and Flüeler, P. (1998). Investigation of Mode III Fracture Toughness Using an Anti-Clastic Plate Bending Method, *Engineering Fracture Mechanics*, **60**: 5–6.
10. Podczeck, F. (2001). The Determination of Fracture Mechanics Properties of Pharmaceutical Materials in Mode III Loading Using an Anti-Clastic Plate Bending Method, *International Journal of Pharmaceutics*, **227**: 39–46.
11. Lee, S.M. (1993). An Edge Crack Torsion Method for Mode III Delamination Fracture Testing, *Journal of Composites Technology and Research*, **15**(3): 193–201.
12. Adams, D.F., Carlsson, L.A. and Pipes, R.B. (2003). *Experimental Characterization of Advanced Composite Materials*, **3rd edn**, CRC Press, Boca Raton, London, New York, Washington.
13. Li, X., Carlsson, L.A. and Davies, P. (2004). Influence of Fiber Volume Fraction on Mode III Interlaminar Fracture Toughness of Glass/Epoxy Composites, *Composites Science and Technology*, **64**: 1279–1286.
14. Suemasu, H. (1999). An Experimental Method to Measure the Mode-III Interlaminar Fracture Toughness of Composite Materials, *Composites Science and Technology*, **59**: 1015–1021.
15. Liao, W.C. and Sun, C.T. (1996). The Determination of Mode III Fracture Toughness in Thick Composite Laminates, *Composites Science and Technology*, **56**: 489–499.
16. de Morais, A.B., Pereira, A.B., de Moura, M.F.S.F. and Magalhães, A.G. (2009). Mode III Interlaminar Fracture of Carbon/Epoxy Laminates Using the Edge Crack Torsion (ECT) Test, *Composites Science and Technology*, **69**: 670–676.
17. Zhao, D. and Wang, Y. (1998). Mode III Fracture Behaviour of Laminated Composite with Edge Crack in Torsion, *Theoretical and Applied Fracture Mechanics*, **29**: 109–123.
18. Ratcliffe, J.G. (2004). Characterization of the Edge Crack Torsion (ECT) Test for Mode III Fracture Toughness Measurement of Laminated Composites, NASA/Technical Memorandum-2004-213269, NASA.
19. Pennas, D., Cantwell, W.J. and Compston, P. (2007). The Influence of Strain Rate on the Mode III Interlaminar Fracture of Composite Materials, *Journal of Composite Materials*, **41**: 2595–2614.
20. de Moura, M.F.S.F., Fernandez, M.V.C., de Morais, A.B. and Campilho, R.D.S.G. (2008). Numerical Analysis of the Edge Crack Torsion Test for Mode III Interlaminar Fracture of Composite Laminates, *Engineering Fracture Mechanics*, **76**(4): 469–478.
21. de Morais, A.B. and Pereira, A.B. (2009). Mode III Interlaminar Fracture of Carbon/Epoxy Laminates Using a Four-Point Bending Plate Test, *Composites Part A: Applied Science and Manufacturing*, **40**: 1741–1746.
22. Williams, J.G. and Hadavinia, H. (2000). Analytical Solutions for Cohesive Zone Models, *Journal of the Mechanics and Physics*, **50**: 809–825.
23. Camanho, P.P. and Dàvila, C.G. (2002). Mixed-Mode Decohesion Finite Elements for the Simulation of Delamination in Composite Materials, NASA/Technical Memorandum-2002-211737, NASA.
24. Szekrényes, A. (2007). Delamination Fracture Analysis in the G_{II}–G_{III} Plane Using Prestressed Transparent Composite Beams, *International Journal of Solids and Structures*, **44**: 3359–3378.
25. Hashemi, S., Kinloch, J. and Williams, J.G. (1990). Mechanics and Mechanisms of Delamination in a Poly(ether sulphone)-Fibre Composite, *Composites Science and Technology*, **37**: 429–462.
26. Szekrényes, A. and Uj, J. (2005). Advanced Beam Model for Fiber-Bridging in Unidirectional Composite Double-Cantilever Beam Specimens, *Engineering Fracture Mechanics*, **72**: 2686–2702.
27. Szekrényes, A. and Uj, J. (2005). Mode-II Fracture in E-glass/Polyester Composite, *Journal of Composite Materials*, **39**(19): 1747–1768.